This article has been accepted for publication in the Journal of Medical Robotics Research Special Issue: Robot-Assisted Surgery and Therapy. Content may change prior to publication.

DOI: 10.1142/S2424905X16400018

Needle Tracking and Deflection Prediction for Robot-Assisted Needle Insertion using 2D Ultrasound Images

Michael Waine[a], Carlos Rossa[a], Ron Sloboda[b], Nawaid Usmani[b], Mahdi Tavakoli[a]

[a] *Department of Electrical and Computer Engineering, University of Alberta, Edmonton, AB, Canada, T6G 2V4*
E-mail: mwaine@ualberta.ca, rossa@ualberta.ca, mahdi.tavakoli@ualberta.ca

[b] *Department of Oncology, University of Alberta, Edmonton, AB, Canada, T6G 1Z2*
Email: ron.sloboda@albertahealthservices.ca, nawaid.usmani@albertahealthservices.ca

In many types of percutaneous needle insertion surgeries, tissue deformation and needle deflection can create significant difficulties for accurate needle placement. In this paper, we present a method for automatic needle tracking in 2D ultrasound images, which is used in a needle-tissue interaction model to estimate current and future needle tip deflection. This is demonstrated using a semi-automatic needle steering system. The ultrasound probe can be controlled to follow the needle tip or it can be stopped at an appropriate position to avoid tissue deformation of the target area. Ultrasound images are used to fully parameterize the needle-tissue model. Once the needle deflection reaches a pre-determined threshold, the robot rotates the needle to correct the tip's trajectory. Experimental results show that the final needle tip deflection can be estimated with average accuracies between 0.7 mm to 1.0 mm for insertions with and without rotation. The proposed method provides surgeons with improved ultrasound feedback of the needle tip deflection and minimizes the motion of the ultrasound probe to reduce tissue deformation of the target area.

Keywords: Needle; Modelling; Tracking; Ultrasound; Prostate; Brachytherapy

1. Introduction

With the rise of minimally invasive surgery and biomedical imaging in the past decades, percutaneous needle insertions have found use in a wide variety of medical applications: anesthesiology,[1] biopsy,[2] brachytherapy,[3] and drainage[4] are just a few examples. Permanent prostate brachytherapy (PPB), the main focus of this paper, is a needle insertion surgery developed in the 1980's as a method to treat early stage prostate cancer.[5] The procedure has shown to have progression-free and cause-specific survival rates of greater than 96% for men with low to intermediate-risk prostate cancer.[6]

A depiction of PPB is shown in Fig. 1. In this procedure, hollow, flexible needles containing radioactive seeds are inserted into the prostate. The needle is monitored using ultrasound (US) imaging to verify placement accuracy. Once the needle is properly positioned, the seeds are permanently deposited within the prostate gland to apply a localized dose of radiation to the area. Therefore, the success of prostate brachytherapy critically depends on accurate placement of the seeds.[7]

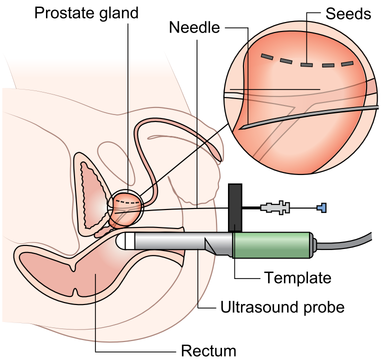

Fig. 1. Depiction of permanent prostate brachytherapy. Needles filled with radioactive seeds are inserted into the prostate gland through a template grid. The seeds are permanently deposited to destroy cancerous tissue. *Image courtesy of Cancer Research UK / Wikimedia Commons.*

Prostate brachytherapy needles are typically 200 mm in length, and are often bevel-tipped so that the needle can slice through soft-tissue while still allowing the brachytherapy seeds to be easily ejected. The bevel causes an imbalance of forces applied to the needle tip as it cuts through tissue, causing the needle to deflect during insertion. These factors, when combined with the effects of tissue deformation, can lead to significant errors in needle placement if corrective steering is not performed.[8]

Typically, during manual PPB surgery, the surgeon monitors a transverse US slice near the maximum insertion depth of the needle. Once the needle has been inserted, a cross-sectional view of the needle appears in the transverse image as shown in the left-hand panel of Fig. 2. If the needle is too far from the pre-planned target position as observed in the US image, the needle is withdrawn and inserted again until the placement error is within the surgeon's tolerance range. The surgeon's ability to steer the needle under limited feedback is critical for minimizing the number of reinsertions required and to deliver the prescribed dose distribution. However, there are no well-defined guidelines for needle steering for these type of procedures, with steering strategies normally developed through empirical observation, experience, and trial-and-error.

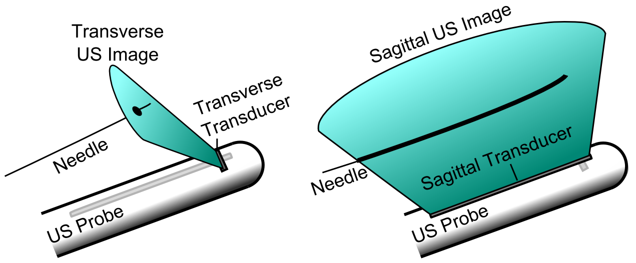

Fig. 2. Example of transverse (left) vs. sagittal (right) US imaging. In transverse images, a cross-section of the needle perpendicular to its neutral axis is observed. In sagittal images, the needle's neutral axis is observed.

US-based needle tracking and needle segmentation strategies have been researched by several different groups. Many have studied segmentation in 3D images or sagittal images, where the images show a portion of the needle's neutral axis as shown in the right-hand panel of Fig. 2. For example, needle segmentation using the Radon/Hough transform has been studied in [9–11]. Another widely used technique for needle or surgical tool segmentation in US is random sample consensus, as shown in [12–14]. Other techniques include Gabor filtering in [15, 16], shape-based level set methods in [17] and the use of a specific feature set as described in [18]. However, in PPB for example, the transrectal probe's movement is limited by the rectum, preventing reliable use of sagittal images. The needle may deflect in a plane that is impossible to observe using sagittal imaging, given the restrictions imposed by the rectum. Another limitation of sagittal imaging is that it is difficult to use during needle insertion due to the unpredictable path the needle may follow. With respect to 3D US, the images and videos generated result in very large data sets which can cause difficulties for real-time needle steering. As well, the majority of clinical 3D US machines are sweep-based, which is generally slow and again, undesirable for real-time systems.

Transverse US imaging can be used regardless of the needle's deflection plane, unlike sagittal images. As well, clinical PPB equipment and software are well-suited for transverse US imaging. Needle segmentation in transverse US has been studied by a few groups, such as [19], where a voice coil actuator and Doppler US is used, and [20] where morphological image processing and Hough transform-based feature extraction algorithm is employed. Both of these techniques rely on a comet tail artifact being observable in the US image, which is a form of reverberation artifact in US images caused by highly reflective surfaces, like the needle. In biological tissue, the needle's comet tail artifact is not always visible using B-mode US, and extraneous objects such as calcifications and air pockets can appear very similar to the needle.

Several US-guided needle steering robots have been developed, including those that apply external forces to the needle base for steering correction,[21–23] and rotation-based needle steering devices.[20, 24] Additionally, a similar Doppler US segmentation method as in [19] has been used for rotation-based needle steering.[25]

All of these methods require the position of the US probe to be adjusted such that the needle tip is always located within the field of view of the US images. This is particularly problematic for prostate brachytherapy, where movement of the US probe can deform the prostate and shift the target location. Therefore, limiting the movement of the US probe is desirable.

In this paper, we present a method to assist surgeons during needle insertion procedures by providing reliable needle tracking in US images and reducing movement of the US probe. This is demonstrated using a semi-automatic needle steering system. The needle insertion procedure is divided into two consecutive phases. In the first phase, the US probe and the needle move in tandem, such that the needle tip is constantly in the field of view of the US images. In order to track the needle in the US images, we developed a threshold-based image processing algorithm combined with Kalman filtering. Once the needle is located in the US images, the information is used to parameterize a needle-tissue interaction model that is used to estimate future needle tip deflection. The needle is rotated once the current tip deflection reaches a user-specified threshold. In the second phase of the insertion, the US probe stops while the needle continues to be inserted. This is to prevent the US probe from applying force to tissue and critical structures found at or near the target area. It is assumed that needle rotation occurs before the probe stops moving, and that a single rotation at an appropriate depth is used to correct the trajectory of the needle.

The contributions of this paper include the development of a robust needle tracking method based on image processing, Kalman filtering and a needle-tissue interaction model that relies solely on 2D US feedback for parametrization without the need for tissue characterization. In addition, our method allows the US probe to be stopped at a desired depth in order to avoid tissue deformation caused by US probe contact. The method is demonstrated using biological tissue experiments and a basic threshold-based needle steering system. The rest of the paper is as follows. In Section 2, the needle-tracking algorithm is defined. The model for needle tip trajectory prediction is outlined in Section 3. In Section 4, the biological experiments and the experimental setup is described. Results are shown in Section 5 and are discussed in Section 6. Conclusions are summarized in Section 7.

2. Real-time Needle Tracking in US Images

In this section, the method for real-time needle tracking is described. Our setup continuously receives transverse US images of the needle. In transverse images, a cross-section of the needle is shown, such that the needle appears as a bright, elliptical object, as shown in Fig. 3.

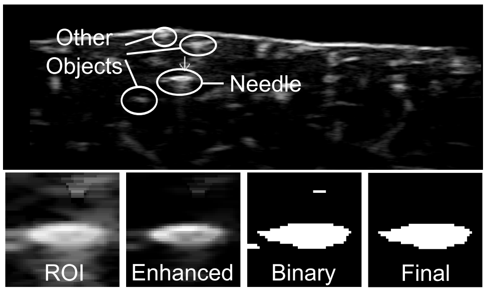

Fig. 3. An image of the needle embedded within biological tissue. The needle and extraneous background objects are shown. Underneath, the image processing steps are shown.

Before the needle insertion begins, the insertion location is manually identified. This is used to define an initial region of interest (ROI). In our study, this ROI is set to a 2.5 mm x 2.5 mm window centered around the needle's insertion location. The ROI is shown in Fig. 3.

2.1. *Image Processing*

After initializing the ROI, as shown in the panel of Fig. 3 labelled ROI, we apply contrast stretching in order to improve contrast between the bright needle pixels and the dark background tissue. The image processing method is an extension of our past work.[26] The contrast stretching equation is given by:

$$T(r) = \left(\frac{I - 0.1I_{max}}{I_{max} - 0.1I_{max}}\right)^{\gamma} \tag{1}$$

where I represents the normalized ROI image with pixel intensities ranging from $[0, 1]$. The pixel intensity zero represents the color black and one represents the color white. The values I_{max} corresponds to the normalized maximum intensity values present within the original ROI. The value of γ is used to define the shape the exponential curve mapping the intensity values from the original ROI to the transformed ROI.[27] We set $\gamma = 2$, which weights darker pixels more heavily. The result of (1) is a one-sided saturation of the lower-intensity background pixels followed by an exponential contrast enhancement. An example of the enhanced ROI is shown in Fig. 3 in the panel labelled Enhanced.

After enhancing the ROI, its cumulative histogram is used to determine an appropriate intensity threshold. The intensity threshold is chosen based on the number of pixels n within the ROI expected to correspond to the needle, which is obtained from 2:

$$n = \frac{\beta A I_{max}}{I_{dx} I_{dy}} \tag{2}$$

where A is the area of the needle's cross section in mm^2, I_{dx} and I_{dy} represent the height and width dimensions of a single pixel in the ROI in mm, respectively, and β is a manually selected parameter used to account for needle distortion caused by attenuation, diffraction and diffusion of the US beam. In our work, β was set to 0.75 based on empirical tests. The intensity threshold selected for the ROI is that in which at least n pixels lie above the threshold. I_{max} is also used to modify the expected number of needle pixels. When I_{max} is low, the needle is less visible, and so the expected number of needle pixels is decreased to compensate. After the threshold is applied, the result is a binary image, as shown in Fig. 3 in the panel labelled Binary.

After thresholding is completed, any cluster of needle point candidates with fewer than 20% of n connected components are removed. After all image processing steps have been performed, we obtain a set of needle point candidates as shown in Fig 3 in the panel labelled Final. A Kalman filtering algorithm is used to filter outliers from the set of candidate points, as well as deal with other issues described in the next section.

2.2. *Kalman Filtering*

The Kalman filter has been successfully used for needle tracking in [13, 14, 20, 28]. In this paper, we use it not only to help improve the needle estimation, but to help remove outliers from the ROI, such as air bubbles, or tissue inhomogeneities, which can often be mistaken for the needle when performing insertions into biological tissue. As well, sometimes whether due to loose contact between the probe and the tissue, or due to extreme attenuation of the needle, the needle appears with very poor visibility within the ROI such that it can not be found with the traditional image processing steps described above. The Kalman filter is used to predict where the needle should be within the ROI given the needle's historical trajectory. After Kalman filtering, the ROI for the next iteration is updated by centering the ROI around the updated needle position estimate.

It is assumed that the change in needle tip position is constant between successive frames. The state prediction $\hat{\boldsymbol{x}}_{k|k-1}$ is the prediction of the needle tip position x and y and the change in tip position x' and y' at sample k given the state results from the previous iteration where the state $\boldsymbol{x}$ is:

$$\boldsymbol{x}_k = \begin{bmatrix} x_k \\ y_k \\ x'_k \\ y'_k \end{bmatrix} \tag{3}$$

The state prediction at sample k given the sample at $k-1$ is calculated as follows:

$$\hat{\boldsymbol{x}}_{k|k-1} = F\hat{\boldsymbol{x}}_{k-1} \tag{4}$$

where F is the state transition model used to calculate the state prediction. The state transition model is given by:

$$F = \begin{bmatrix} 1 & 0 & \Delta d & 0 \\ 0 & 1 & 0 & \Delta d \\ 0 & 0 & 1 & 0 \\ 0 & 0 & 0 & 1 \end{bmatrix} \tag{5}$$

where Δd represents the change in depth between successive US frames.

During cases where there are multiple objects present within the ROI, the state prediction $\hat{\boldsymbol{x}}_{k|k-1}$ is used to detect outliers. The needle location is estimated using (4). Any needle point candidates within a window of 110% of the outer needle diameter are considered inliers, and points outside of this window are ignored.

If the needle can be located within the ROI, the measured needle location $\mathbf{z_k}$ is obtained using (6).

$$\boldsymbol{z}_k = \begin{bmatrix} \mathrm{med}(x_{in}) \\ \mathrm{med}(x_{in}) \\ \frac{\Delta x_N}{\Delta d_N} \\ \frac{\Delta y_N}{\Delta d_N} \end{bmatrix} \tag{6}$$

where x_{in} and y_{in} are the inlying needle point candidates, $\mathrm{med}(\cdot)$ is the median operator, d_N is the change in depth over the past N frames, and x_N and y_N are the change in tip positions along the x and y axes, respectively, over the past N frames. The median is used rather than the mean as another method to protect against outliers.

After obtaining the measurements $\mathbf{z_k}$ from the US images, the needle location is updated using the Kalman filter to obtain the updated state estimation $\hat{\boldsymbol{x}}_{k|k}$, based on the state vector results obtained from the previous iteration using the following equation:

$$\hat{\boldsymbol{x}}_{k|k} = \hat{\boldsymbol{x}}_{k|k-1} + K_k\boldsymbol{z}_k \tag{7}$$

where K_k is the Kalman gain, which is related to the degree of correction caused by the incoming measurements $\mathbf{z_k}$. The Kalman gain is calculated using:

$$K_k = P_{k|k-1}H_k^T S_k^{-1} \tag{8}$$

where $\hat{\boldsymbol{P}}_{k|k-1}$ is the co-variance error of the state prediction $\hat{\boldsymbol{x}}_{k|k-1}$, H is the measurement model used to define the states that are being measured at each sample k, and S_k is the covariance of the residuals, which is related to the variability in $\mathbf{z_k}$. The equation for $\hat{\boldsymbol{P}}_{k|k-1}$ is given by:

$$\hat{\boldsymbol{P}}_{k|k-1} = F\hat{\boldsymbol{P}}_{k-1}F^T + Q \tag{9}$$

where Q is the process noise covariance matrix. The residual covariance S_k and the measurement model H are given by the following equations:

$$S_k = H_k P_{k|k-1} H_k^T + R \tag{10}$$

$$H_k = [\, I_{4\times 4} \,] \tag{11}$$

where R is the measurement noise covariance.

The end result of the Kalman filtering procedure is an improved estimation of the needle location based on the past observations of needle trajectory. The ROI for the next iteration of the needle tracking procedure is centered around this improved estimation of the needle tip position. In the event that the needle cannot be located within the ROI for brief periods of time, the state prediction $\hat{\boldsymbol{x}}_{k|k-1}$ is used to predict the needle location and update the ROI so that the needle can continue to be tracked once it reappears. In this case, the updated state estimation $\hat{\boldsymbol{x}}_{k|k}$ is carried over from the previous iteration. In the event that multiple objects are present in the ROI, the state prediction $\hat{\boldsymbol{x}}_{k|k-1}$ is used to determine where the needle should be found within the ROI. Objects lying outside a radius of 110% of the needle's outer radius are considered to be outliers and are removed from the image.

3. Needle Modelling and Needle Tip Deflection Prediction

In addition to needle tracking, we require the ability to estimate the future needle tip deflection. As well, as discussed previously, in the second phase of our needle insertion procedure the probe is stopped while the needle continues to be inserted. In this situation, we need a model for estimating the current needle tip deflection along with the future tip deflection. Needle modeling, insertion and steering within soft-tissue is a popular research topic.[29] Mechanics-based elastic beam models with virtual springs have been widely used for needle steering in [22, 24, 30, 31]. As well, a finite-element method with potential force-fields for needle steering and motion planning has been developed in [32, 33].

These models require accurate characterization of tissue, which is difficult to obtain during *in-vivo* procedures. Here, we propose a simple needle-tissue interaction model that can be completely parameterized using the US-based needle deflection feedback described in the previous section. Euler-Bernoulli beam theory is used in this paper to identify forces applied to an elastic beam, from which the beam's shape can be identified.

The brachytherapy needle can be modelled as a hollow, cylindrical cantilever beam. The needle's deflection can be modelled as a beam with a point load applied to the tip to represent the cutting force applied to the bevel, and second point load applied to the middle of the length inserted into tissue to represent the force exerted by the tissue. An example is shown in Fig. 4.

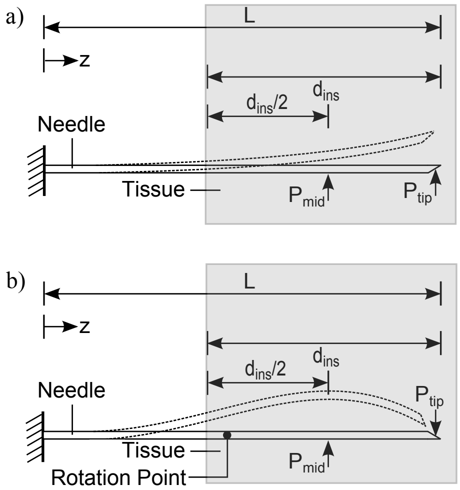

Fig. 4. Needle shape modeling based on point loads applied to a cantilever beam. a) Needle shape before rotation. b) Needle shape after rotation. P_{tip} represents the force applied to the needle tip. P_{mid} represents the force applied to the middle of the inserted needle length.

The beam's shape can be derived from the bending moment $M(z)$ applied at a distance z from the base of the beam. The bending moment equation is given by:

$$M(z) = EI\frac{d^2\delta}{dz^2} \tag{12}$$

where E is the modulus of elasticity of the beam, I is the area moment of inertia of the beam, and δ is the deflection of the beam at a distance z. For a beam with the point loads applied as in Fig. 4, $M(z)$ is equal to:

$$M(z) = P_{tip}(L - z) + P_{mid}\langle \alpha - z \rangle \tag{13}$$

where

$$\alpha = L - \frac{d_{ins}}{2} \tag{14}$$

P_{tip} and P_{mid} represent the forces applied to the needle tip and the centre of the inserted needle depth d_{ins} respectively, L is the needle length, and the function $< \cdot >$ represents the singularity function:

$$< A - B >= \begin{cases} 0, & \text{if} A \leq B \\ A - B, & \text{if} A > B \end{cases} \tag{15}$$

The integral of (13) is the slope $\theta(z)$ of the beam at a distance z:

$$\theta(z) = \frac{1}{2EI}[P_{tip}z(2L - z)] + \frac{1}{2EI}P_{mid}[\alpha^2 - \langle \alpha - z \rangle^2] \tag{16}$$

Integrating (16) allows us to solve for the deflection of the beam:

$$y(z) = \frac{1}{6EI}[P_{tip}z^2(3L - z) + P_{mid}(3\alpha^2 z - \alpha^3 + \langle \alpha - z \rangle^3)] \tag{17}$$

Assume that the beam deflection y_d and the slope θ_d at a distance $z = d$ along the beam is known from the US image processing algorithm described in the previous section and $d > \frac{d_{max}}{2}$, where d_{max} is the maximum insertion depth. Then using (16) and (17), we can solve for P_{tip} and P_{mid}:

$$P_{tip} = 2EI\frac{3y_d + a\theta_d - 3d\theta_d}{d\,(2L\alpha - 3Ld - \alpha d + 2d^2)} \tag{18}$$

$$P_{mid} = \frac{P_{tip}d^2 - 2LP_{tip}d + 2\theta_d EI}{\alpha^2} \tag{19}$$

Using (17)-(19) we can solve for the needle's deflection along the beam. In our case, for the first phase of the insertion, when the US probe follows the needle tip, the deflection and slope at the needle tip is known. In the second phase of the insertion, when the US probe stops moving while the needle continues to be inserted, the deflection is known, and the slope at the observed depth is assumed to remain constant relative to the last measured slope obtained from the first phase.

In order to predict the tip trajectory at the maximum depth d_{max}, the beam is extrapolated by a length of a, where a is the difference between the maximum depth and the current depth of the needle. Before the needle is rotated (or in the case where no rotation occurs), the extrapolated segment of the beam is represented with a first-order polynomial with a slope equal to the slope of the needle tip. After rotation, due to the added flexion of the beam, the extrapolated segment of the beam is represented with a curve of constant radius, which is fitted to the portion of the beam found after the rotation depth.

The end result is a needle-tissue interaction model based on Euler-Bernoulli beam theory, which can be used for prediction of the needle tip position at the maximum depth. The model itself is parameterized solely using US image feedback, which is beneficial for *in-vivo* procedures, since there is no need to obtain tissue characteristics for each new patient.

4. Experimental Setup

We used a version of the the needle insertion device demonstrated in [34] for our needle insertion experiments. An image of the device is shown in Fig. 5. The needle is mounted on a two degree-of-freedom system consisting of a prismatic joint allowing for needle insertion along the z-axis and a revolute joint allowing for needle rotation about the z-axis. The prismatic joint is controlled with a Maxon RE40 DC motor and the revolute joint is controlled with a Maxon RE25 1:14 geared motor (Maxon Motor AG, Sachseln, Switzerland). The revolute joint is directly coupled to the motor, while the prismatic joint consists of a ball bearing-mounted carriage system attached to a motorized belt, which allows for control of the needle's insertion velocity. The motors are controlled with a Humusoft MF624 DAQ card which interfaces to a PC via PCI.

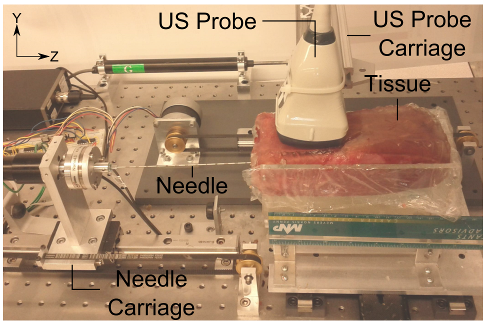

Fig. 5. Needle insertion setup. The needle and probe are attached to separate motorized carriages. The probe moves with the same velocity as the needle up to a specified depth. Afterwards, the needle continues while the probe remains stationary.

A separate prismatic joint is attached to a translating stage, which is used to mount the US probe. The joint is controlled through a separate motor, which allows the US probe to move independently of needle. The insertion procedure can be separated into two consecutive phases. In the first phase, the needle can be inserted either manually or with a constant velocity. The velocity of the US probe is matched to the needle's velocity so that the needle tip is constantly observed in the US images. In the second phase, the velocity of the US probe carriage is set to zero while the needle continues to be inserted. This is to allow for monitoring of the needle without affecting movement of critical targets caused by force applied by the US probe. Fig. 6 shows how the velocity of the US probe is controlled during the different phases of the needle insertion procedure. The position of the needle carriage and the US probe are measured, and the velocities are controlled using a PID controller. During the first phase, the desired velocity of the US probe carriage is equal to the measured velocity of the needle carriage. During the second phase, the velocity of the US probe carriage is set to zero. If the needle is instead inserted manually, the PID controller is only used to control the US probe carriage.

US images are collected using a SonixTouch Ultrasound System (Analogic Ultrasound, Richmond, BC, Canada) and a linear US transducer model 4DL14-5/38 (Analogic Ultrasound, Richmond, BC, Canada). A DVI-to-USB 3.0 frame grabber (Epiphan, Palo Alto, CA, USA) transfers the images from the US machine to a PC for processing at a frame rate of 20 Hz.

The needle used for the experiments is an 18 gauge, bevel-tipped brachytherapy needle, model PSS1820EZ (Worldwide Medical Technologies, Oxford, CT, USA). Fresh, *ex-vivo* beef tissue was used for the offline experiments described in Section 5.1. For the online experiments described in Section 5.2, a beef tissue phantom with an initial 20 mm layer of gelatin to simulate the effects of multiple tissue layers and internal tissue interfaces was used. After consulting with brachytherapy surgeons, beef tissue was identified as being most similar from a surgeon's perspective to the tissue encountered before reaching the prostate. However, the development of a more anatomically correct tissue phantom for simulation of the tissue layers encountered in prostate brachytherapy and similar surgical procedures is a topic that we will further explore in future work.

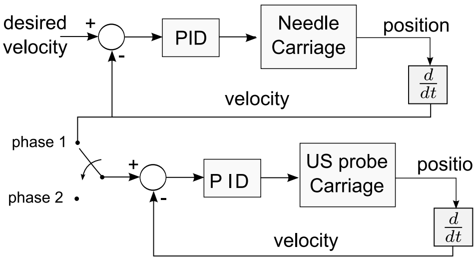

Fig. 6. Block diagram showing how the US probe is controlled through phases 1 (where the probe follows the needle tip) and 2 (where the probe stops while the needle continues) of the needle insertion procedure.

During the first phase of the insertion, the US probe follows the needle tip. The deflection of the needle tip is monitored via the US images. The needle rotates once the resultant magnitude of deflection in the x and y planes (δ_x and δ_y respectively) reaches a threshold ϵ. At this point, the needle rotates by an amount ϕ defined by (20):

$$\phi = 180^\circ + \arctan\left(\frac{\delta_y}{|\delta_x|}\right) \tag{20}$$

where $\phi = 0^\circ$ represents the angle where the needle bevel is aligned with the x plane such that needle deflection occurs in the $+x$ direction under ideal conditions. Before insertion begins, the needle is always aligned to the $\phi = 0°$ position. Eqn. (20) allows us to counteract some of the minor out-of-plane deflection caused by tissue motion or insertion angle.

5. Experimental Results

First, we validated the needle tip prediction model using offline experiments, where the needle insertion velocity is controlled by the robot. Then, we performed online experiments where the needle is manually inserted, and a threshold-based controller is used to compensate for needle deflection once it reaches the specified threshold.

5.1. *Prediction of Needle Deflection*

Offline experiments are performed with the probe positioned at the needle tip throughout the entire trial. Insertion trials without rotation are performed at constant velocities of 5, 10, 20, and 30 mm/s and insertion trials with rotation are performed at a constant velocity of 5 mm/s, with the needle being rotated after an insertion depth of 40 mm or 80 mm, for a total of 48 insertion trials all together. In all trials, the needles are inserted to a depth of 140 mm. The needle tip is tracked for each trial offline using the procedure outlined in Section 2 and the needle's trajectory is predicted using the equations developed in Section 3.

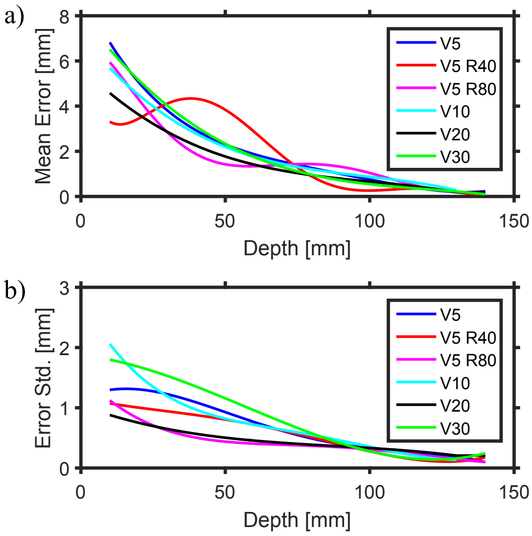

Fig. 7. Comparison of the predicted needle tip deflection error relative to the actual final tip deflection as a function of the maximum depth observed by the US probe. The (a) mean and (b) standard deviation of the prediction error are shown.

In the next section, we will use a threshold-based controller to compensate for needle deflection in real-time.

5.2. *Online Needle Tip Prediction and Steering*

Preliminary experiments are shown in Fig. 8. As can be seen, the depth of rotation is a strong determinant of the final needle deflection. If the needle is rotated early during the needle insertion process such as at 40 mm, when the needle has not yet deflected a significant amount, the final tip deflection results in a 60% decrease in deflection compared to the case with no rotation. When the needle is rotated relatively late during insertion such as at 80 mm, the final needle tip deflection does not result in a significant difference compared to the case with no rotation. The needle must rotate relatively early during the insertion in order to have a noticeable impact on tip deflection. Therefore, the value for the deflection threshold ϵ must be relatively small in order to influence the tip deflection by a useful margin. We selected a deflection threshold of $\epsilon = 2$ mm to demonstrate how our needle deflection prediction method could be integrated with a needle steering system. This threshold was chosen based on empirical results observed in test trials by our group, as well as the results obtained in [35]. Future work will focus on developing more robust control algorithms for use with the deflection algorithm presented here.

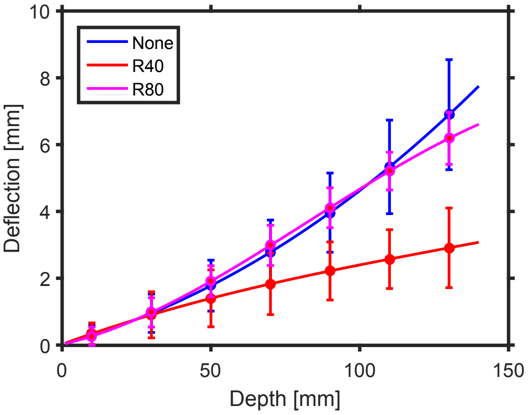

Fig. 8. Comparison of needle tip deflection for cases with rotation at a depth of 40 mm (R40), 80 mm (R80) and without rotation (None). The needles were inserted at a velocity of 5 mm/s to a depth of 140 mm. The error bars show the standard deviation calculated for each case.

Fifteen needle insertion trials are performed with steering and fifteen are performed without steering for a total of 30 trials in total. The tip deflection prediction results for each are compared. The needle is inserted manually to a depth of 140 mm. The US probe moved in tandem with the needle tip up to a depth of 90 mm, which was selected based on the results of the offline deflection experiments. For cases with needle steering, the needle rotates after a deflection threshold of $\epsilon = 2$ mm. Boxplot comparisons of the final tip deflection for the cases with and without needle steering are shown in Fig. 9. The use of steering decreased the final tip deflection from an average of 10 mm to an average of 3.7 mm.

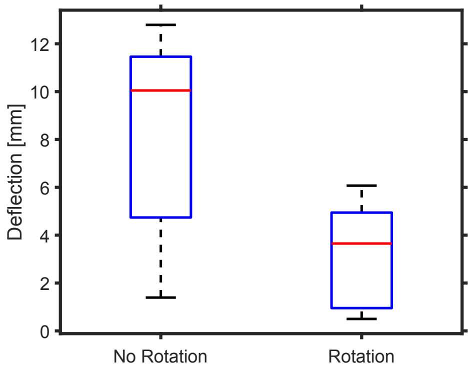

Fig. 9. Comparison of the final tip deflection with respect to cases with no needle steering (No Rotation) and the cases with needle steering (Rotation).

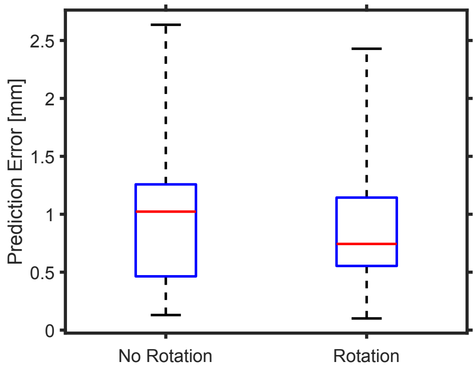

Fig. 10. Comparison of the prediction error with respect to cases with no needle steering (No Rotation) and the cases with needle steering (Rotation). The prediction error represents the absolute difference between the final predicted needle tip deflection and the true tip deflection.

Boxplot comparisons of the prediction error between the predicted needle tip deflection at the end of the insertion and the actual needle tip deflection at the end of the insertion are shown in Fig. 10. For cases without rotation, the needle can be predicted with a median accuracy of 1.0 mm, with accuracies ranging from 0.1 mm to 2.6 mm. For cases with rotation, the needle can be predicted with a median accuracy of 0.7 mm, with accuracies ranging from 0.1 mm to 2.4 mm.

6. Discussion

Fig. 7 shows the error between the final predicted tip deflection and the actual tip deflection as a function of the US probe's final observed depth. V5, V10, V20 and V30 represent insertions performed at constant velocities of 5 mm/s, 10 mm/s, 20 mm/s, and 30 mm/s respectively. V5 R40 and V5 R80 represent insertions performed at a velocity of 5 mm/s with rotations performed at a depth of 40 mm and 80 mm respectively.

As observed in Fig. 7, both the mean and standard deviation of the prediction error generally decreases the longer that the needle tip is observed over the course of the insertion. When the needle tip is observed to a depth of 70 mm onwards, the needle tip deflection can be predicted with an accuracy of 1.8 ± 1.6 mm for all cases except the V5 R40 case. From depths of 90 mm onwards, the needle tip deflection can be predicted with an accuracy of 1.3 ± 1.0 mm for all cases. For cases with rotation, the needle must be observed at depths greater than the rotation depth in order to predict the tip deflection with an accuracy of less than 2 mm.

The online experiments show that the needle tip deflection can be predicted with an average error of less than 1.0 mm when the probe is stopped at a depth of 90 mm or 64% of the maximum insertion depth. These errors are smaller than the 5 mm placement accuracy of experienced physicians.[36]

In current PPB practices, the probe is typically positioned at or near the desired insertion depth. The needle must be fully inserted before needle placement can be assessed. If the needle is placed too far from the target location, the needle must be withdrawn and re-inserted. This process of performing multiple re-insertions to obtain satisfactory needle placement can cause increased tissue trauma and swelling. By moving the US probe in tandem with the needle at the beginning of the insertion, the surgeon can accurately monitor the needle's deflection well before the maximum insertion depth. This allows them to decide well in advance of the maximum insertion depth whether a re-insertion would be necessary. In addition, through the use of an appropriate needle steering algorithm, the needle can be automatically rotated to consistently reduce needle tip deflection, preventing the need for re-insertions in the first place.

In addition, stopping the US probe before the desired insertion depth at the second phase of the insertion procedure is highly beneficial, as tissue motion of the target area caused by force applied by the US probe is reduced. For transrectal US-guided procedures, the probe does not need to be inserted far in the patient quite so often using the proposed method, which should help simplify the procedure by minimizing movement of the probe. This system holds great potential for US-guided percutaneous needle insertion procedures where the needle must travel a significant length into the body, such as prostate brachytherapy or biopsy of deep tissues.

Since the needle-tissue interaction model is parameterized solely based on US image feedback, the needle must be rotated before the probe stops moving, such that the needle tip's new trajectory can be properly estimated. This limitation is not overly restrictive, however, since based on Fig. 8, the needle must rotate early during the insertion process in order to have a significant impact on needle deflection. Another limitation is that the model currently accounts for single rotations, not multiple rotations. As well, the threshold-based needle steering control algorithm was a simple control algorithm used to demonstrate how our needle tracking and needle prediction methods can be used in practice. Further study on rotation-based control for needle steering is a topic for future investigation. Finally, the beef tissue phantoms used in this study simulated only the tissue encountered before reaching the prostate. Future work will explore the development of more anatomically correct tissue phantoms.

7. Conclusion

In this paper, a method for automatic needle tracking in US images and needle tip deflection prediction is presented and is demonstrated with a semi-automatic needle steering system. A threshold-based image processing algorithm is combined with Kalman filtering to develop a robust needle tracking procedure for use with transverse US images. The needle tracking results are used to fully parameterize a needle-tissue interaction model. The model is then used to predict future tip deflection. The semi-automatic needle steering procedure is divided into two consecutive phases. In the first phase, the US probe is moved in tandem with the needle such that the needle tip is constantly in the field of view of the US images. In the second phase of the procedure, the US probe stops while the needle continues to be inserted in order to prevent the probe from applying unnecessary forces to deeper tissue and structures.

Results showed that for cases without rotation, the needle tip deflection can be predicted with an average accuracy of 1.0 mm, ranging from 0.1 mm to 2.6 mm. For cases with rotation, the needle can also be predicted with an average accuracy of 0.7 mm, ranging from 0.1 mm to 2.4 mm.

This system can be of great aid to surgeons performing deep percutaneous needle insertion procedures such as prostate brachytherapy. In the first phase of the procedure, the US feedback can provide information for the surgeon about future tip deflection so that they can determine the accuracy of the needle placement. In the second phase of the procedure, the US probe can stop to prevent applying tissue forces to the target area while providing the surgeon with an accurate estimation of the current and future needle tip deflection.

Acknowledgments

This work was supported by the Natural Sciences and Engineering Research Council (NSERC) of Canada under grant CHRP 446520, the Canadian Institutes of Health Research (CIHR) under grant CPG 127768, and by the Alberta Innovates - Health Solutions (AIHS) under grant CRIO 201201232.

References

[1] P. Marhofer and V. W. Chan, Ultrasound-guided regional anesthesia: current concepts and future trends, *Anesthesia & Analgesia* **104**(5) (2007) 1265–1269.

[2] A. D'Amico, C. Tempany, R. Cormack, N. Hata, M. Jinzaki, K. Tuncali, M. Weinstein and J. Richie, Transperineal magnetic resonance image guided prostate biopsy, *The Journal of urology* **164**(2) (2000) 385–387.

[3] B. J. Davis, E. M. Horwitz, W. R. Lee, J. M. Crook, R. G. Stock, G. S. Merrick, W. M. Butler, P. D. Grimm, N. N. Stone, L. Potters *et al.*, American Brachytherapy Society consensus guidelines for transrectal ultrasound-guided permanent prostate brachytherapy, *Brachytherapy* **11**(1) (2012) 6–19.

[4] J. Hong, T. Dohi, M. Hashizume, K. Konishi and N. Hata, An ultrasound-driven needle-insertion robot for percutaneous cholecystostomy, *Physics in Medicine and Biology* **49**(3) (2004) p. 441.

[5] K. K. Charyulu, Transperineal interstitial implantation of prostate cancer: a new method, *International Journal of Radiation Oncology* Biology* Physics* **6**(9) (1980) 1261–1266.

[6] A. V. Taira, G. S. Merrick, R. W. Galbreath, K. E. Wallner and W. M. Butler, Natural history of clinically staged low-and intermediate-risk prostate cancer treated with monotherapeutic permanent interstitial brachytherapy, *International Journal of Radiation Oncology* Biology* Physics* **76**(2) (2010) 349–354.

[7] L. Potters, C. Morgenstern, E. Calugaru, P. Fearn, A. Jassal, J. Presser and E. Mullen, 12-year outcomes following permanent prostate brachytherapy in patients with clinically localized prostate cancer, *The Journal of urology* **173**(5) (2005) 1562–1566.

[8] G. Wan, Z. Wei, L. Gardi, D. B. Downey and A. Fenster, Brachytherapy needle deflection evaluation and correction, *Medical Physics* **32**(4) (2005) 902–909.

[9] H. R. S. Neshat and R. V. Patel, Real-time parametric curved needle segmentation in 3D ultrasound images, *Biomedical Robotics and Biomechatronics, 2008. BioRob 2008. 2nd IEEE RAS & EMBS International Conference on*, IEEE (2008), pp. 670–675.

[10] P. M. Novotny, J. A. Stoll, N. V. Vasilyev, J. Pedro, P. E. Dupont, T. E. Zickler and R. D. Howe,

GPU based real-time instrument tracking with three-dimensional ultrasound, *Medical image analysis* **11**(5) (2007) 458–464.

[11] S. H. Okazawa, R. Ebrahimi, J. Chuang, R. N. Rohling and S. E. Salcudean, Methods for segmenting curved needles in ultrasound images, *Medical image analysis* **10**(3) (2006) 330–342.

[12] M. Uhercik, J. Kybic, H. Liebgott and C. Cachard, Model fitting using RANSAC for surgical tool localization in 3-D ultrasound images, *Biomedical Engineering, IEEE Transactions on* **57**(8) (2010) 1907–1916.

[13] Y. Zhao, H. Liebgott and C. Cachard, Tracking micro tool in a dynamic 3D ultrasound situation using kalman filter and ransac algorithm, *Biomedical Imaging (ISBI), 2012 9th IEEE International Symposium on*, IEEE (2012), pp. 1076–1079.

[14] Y. Zhao, H. Liebgott and C. Cachard, Tracking biopsy needle using Kalman filter and RANSAC algorithm with 3D ultrasound, *Proceedings of the Acoustics 2012 Nantes Conference*, (2012), pp. 231–236.

[15] M. Kaya and O. Bebek, Needle localization using gabor filtering in 2D ultrasound images, *Robotics and Automation (ICRA), 2014 IEEE International Conference on*, IEEE (2014), pp. 4881–4886.

[16] M. Kaya and O. Bebek, Gabor filter based localization of needles in ultrasound guided robotic interventions, *Imaging Systems and Techniques (IST), 2014 IEEE International Conference on*, IEEE (2014), pp. 112–117.

[17] P. Yan, J. C. Cheeseborough and K. C. Chao, Automatic shape-based level set segmentation for needle tracking in 3-D TRUS-guided prostate brachytherapy, *Ultrasound in medicine & biology* **38**(9) (2012) 1626–1636.

[18] K. Mathiassen, D. Dall'Alba, R. Muradore, P. Fiorini and O. J. Elle, Real-time biopsy needle tip estimation in 2D ultrasound images, *Robotics and Automation (ICRA), 2013 IEEE International Conference on*, IEEE (2013), pp. 4363–4369.

[19] J. D. Greer, T. K. Adebar, G. L. Hwang and A. M. Okamura, Real-time 3D curved needle segmentation using combined B-mode and power doppler ultrasound, *Medical Image Computing and Computer-Assisted Intervention - MICCAI 2014*, (Springer, 2014), pp. 381–388.

[20] G. J. Vrooijink, M. Abayazid, S. Patil, R. Alterovitz and S. Misra, Needle path planning and steering in a three-dimensional non-static environment using two-dimensional ultrasound images, *The International Journal of Robotics Research* (2014) 1–14.

[21] G. Fichtinger, J. P. Fiene, C. W. Kennedy, G. Kronreif, I. Iordachita, D. Y. Song, E. C. Burdette and P. Kazanzides, Robotic assistance for ultrasound-guided prostate brachytherapy, *Medical image analysis* **12**(5) (2008) 535–545.

[22] Z. Neubach and M. Shoham, Ultrasound-guided robot for flexible needle steering, *Biomedical Engineering, IEEE Transactions on* **57**(4) (2010) 799–805.

[23] D. Y. Song, E. C. Burdette, J. Fiene, E. Armour, G. Kronreif, A. Deguet, Z. Zhang, I. Iordachita, G. Fichtinger and P. Kazanzides, Robotic needle guide for prostate brachytherapy: clinical testing of feasibility and performance, *Brachytherapy* **10**(1) (2011) 57–63.

[24] M. Abayazid, R. J. Roesthuis, R. Reilink and S. Misra, Integrating deflection models and image feedback for real-time flexible needle steering, *Robotics, IEEE Transactions on* **29**(2) (2013) 542–553.

[25] T. K. Adebar, A. E. Fletcher and A. M. Okamura, 3-D ultrasound-guided robotic needle steering in biological tissue, *Biomedical Engineering, IEEE Transactions on* **61**(12) (2014) 2899–2910.

[26] M. Waine, C. Rossa, R. Sloboda, N. Usmani and M. Tavakoli, 3D shape visualization of curved needles in tissue from 2D ultrasound images using ransac, *Robotics and Automation (ICRA), 2015 IEEE International Conference on*, IEEE (2015), pp. 4723–4728.

[27] R. C. Gonzalez, R. E. Woods and S. L. Eddins, *Digital Image Processing Using MATLAB* (Prentice Hall Press, Upper Saddle River, NJ, USA, 2007).

[28] P. Chatelain, A. Krupa and M. Marchal, Real-time needle detection and tracking using a visually servoed 3D ultrasound probe, *Robotics and Automation (ICRA), 2013 IEEE International Conference on*, IEEE (2013), pp. 1676–1681.

[29] N. Abolhassani, R. Patel and M. Moallem, Needle insertion into soft tissue: A survey, *Medical engineering & physics* **29**(4) (2007) 413–431.

[30] N. Abolhassani and R. Patel, Deflection of a flexible needle during insertion into soft tissue, *Engineering in Medicine and Biology Society, 2006. EMBS'06. 28th Annual International Conference of the IEEE*, IEEE (2006), pp. 3858–3861.

[31] R. J. Roesthuis, Y. R. van Veen, A. Jahya and S. Misra, Mechanics of needle-tissue interaction, *Intelligent Robots and Systems (IROS), 2011 IEEE/RSJ International Conference on*, IEEE (2011), pp. 2557–2563.

[32] S. P. DiMaio and S. E. Salcudean, Needle insertion modeling and simulation, *Robotics and Automation, IEEE Transactions on* **19**(5) (2003) 864–875.

[33] S. P. DiMaio and S. Salcudean, Needle steering and motion planning in soft tissues, *Biomedical Engineering, IEEE Transactions on* **52**(6) (2005) 965–974.

[34] T. Lehmann, C. Rossa, N. Usmani, R. Sloboda and M. Tavakoli, A virtual sensor for needle deflection estimation during soft-tissue needle insertion, *Robotics and Automation (ICRA), 2015 IEEE International Conference on*, IEEE (2015), pp. 1217–1222.

[35] T. Lehmann, M. Tavakoli, N. Usmani and R. Sloboda, Force-sensor-based estimation of needle tip deflection in brachytherapy, *Journal of Sensors* **2013** (2013).

[36] R. Taschereau, J. Pouliot, J. Roy and D. Tremblay, Seed misplacement and stabilizing needles in transperineal permanent prostate implants, *Radiotherapy and Oncology* **55**(1) (2000) 59–63.

Michael Waine earned his B.Sc. degree in Electrical Engineering from the University of Alberta in 2012. He is now pursuing a MSc in Electrical Engineering at the University of Alberta. He specializes in biomedical engineering, including topics such as needle tracking and shape estimation using ultrasound images, real-time ultrasound-guided needle steering, and analysis of prostate brachytherapy patient data.

Carlos Rossa received his Engineering and the M.Sc degrees in Mechatronics from the Ecole Nationale d'Ingnieurs de Metz, France, both in 2010, and earned the PhD degree in Mechatronics and Robotics from the University of Paris VI, Paris, France in 2013. He is currently a postdoctoral research fellow with the Department of Electrical and Computer Engineering at the University of Alberta, Edmonton, Canada. Dr. Rossa's current research interests include the design and control of haptic interfaces, actuators and sensors technologies, mechatronics, and medical robotics.

Ron Sloboda received his PhD in Nuclear Physics from the University of Alberta in 1979. He is currently a professor in the Department of Oncology at the University of Alberta. His main research interests are dosimetry and treatment planning for brachytherapy, including the design of clinical studies to obtain patient data that inform model-based dose calculation. Current work is focused on incorporating MRI in the treatment planning, delivery, and evaluation processes, particularly for permanent prostate implants and intracavitary/interstitial cervix treatments.

Nawaid Usmani received his MD from McMaster University in 2001. He is currently an Assistant Professor in the Department of Oncology at the University of Alberta. His main research focus is in prostate brachytherapy, which includes quantifying inaccuracies in current brachytherapy techniques, identifying patient populations at a higher risk of toxicity from this treatment, and finding ways to improve outcomes with brachytherapy implants.

Mahdi Tavakoli is an Associate Professor in the Department of Electrical and Computer Engineering, University of Alberta, Canada. He received his BSc and MSc degrees in Electrical Engineering from Ferdowsi University and K.N. Toosi University, Iran, in 1996 and 1999, respectively. He received his PhD degree in Electrical and Computer Engineering from the University of Western Ontario, Canada, in 2005. In 2006, he was a postdoctoral researcher at Canadian Surgical Technologies and Advanced Robotics (CSTAR), Canada. In 2007-2008, he was an NSERC Post-Doctoral Fellow at Harvard University, USA. Dr. Tavakoli's research interests broadly involve the areas of robotics and systems control. Specifically, his research focuses on haptics and teleoperation control, medical robotics, and image-guided surgery. Dr. Tavakoli is the lead author of Haptics for Teleoperated Surgical Robotic Systems (World Scientific, 2008).